International Journal of Nanomedicine

Dovepress
Taylor & Francis Group

Open Access Full Text Article

ORIGINAL RESEARCH

PAD4 Inhibitor-Loaded Magnetic Fe_3O_4 Nanoparticles for Magnetic Targeted Chemotherapy and Magnetic Resonance Imaging of Lung Cancer

Yu Lu[1,2,*], Xin Wang[1,2,*], Yijiang Jia[1,2], Shuai Zhang[1,2], Jin-Kui Yang[3], Qi Li[3], Yuanming Li[4], Yuji Wang[1,2]

[1]Department of Medicinal Chemistry, College of Pharmaceutical Sciences of Capital Medical University, Beijing, 100069, People's Republic of China; [2]Beijing Area Major Laboratory of Peptide and Small Molecular Drugs, Engineering Research Center of Endogenous Prophylactic of Ministry of Education of China, Beijing Laboratory of Biomedical Materials, Laboratory for Clinical Medicine, Capital Medical University, Beijing, 100069, People's Republic of China; [3]Beijing Key Laboratory of Diabetes Research and Care, Department of Endocrinology and Metabolism, Beijing Diabetes Institute, Beijing Tongren Hospital, Capital Medical University, Beijing, 100730, People's Republic of China; [4]Minimally Invasive Tumor Therapies Center, Beijing Hospital, National Center of Gerontology; Institute of Geriatric Medicine, Chinese Academy of Medical Sciences, Beijing, People's Republic of China

*These authors contributed equally to this work

Correspondence: Yuanming Li; Yuji Wang, Email liyuanming3416@bjhmoh.cn; wangyuji@ccmu.edu.cn

Introduction: Lung cancer is a major health concern worldwide owing to its high incidence and mortality rates. Therefore, identification of new therapeutic targets and strategies for lung cancer is critical for improving patient outcomes. Peptidyl arginine deiminase 4 (PAD4) promotes tumor growth and metastasis by catalyzing the citrullination of histones, making it a potential therapeutic target. Although PAD4 inhibitors have shown potential in the treatment of a variety of tumors, existing PAD4 inhibitors lack sufficient specificity and cause substantial systemic adverse reactions. To overcome these challenges, we developed novel YW403@Fe_3O_4-oxidized carboxymethyl chitosan (OCMC) magnetic nanoparticles (MNPs) that enabled magnetically targeted drug delivery by binding the PAD4 inhibitor YW403 to a ferric oxide magnetic carrier.

Methods: In vitro experiments were conducted using 3-(4,5-dimethylthiazol-2-yl)-2,5-diphenyltetrazolium bromide (MTT) assays, Transwell assays, and flow cytometry to evaluate the activity of the MNPs. In vivo experiments involved magnetic resonance imaging (MRI) assessments and inductively coupled plasma mass spectrometry (ICP-MS) analyses to confirm the tumor targeting and iron metabolism of MNPs. Additionally, immunofluorescence staining was employed to further validate the expression of citrullinated histone H3 (H3cit).

Results: The implementation of this approach enhanced the targeting efficiency of PAD4 inhibitors, consequently reducing the required dosage of chemotherapy and potentially facilitating MRI monitoring. In vitro experiments demonstrated that MNPs exhibited superior activity compared to free drugs when subjected to an applied magnetic field, due to increased uptake of MNPs by tumor cells. In vivo experiments revealed that the application of magnetic fields significantly improved the tumor targeting of MNPs without impacting iron metabolism. By suppressing the expression of citrullinated histone (H3cit), MNPs effectively inhibited tumor growth and metastasis.

Discussion: These findings provide new research ideas for the development of novel anti-tumor nanomaterials and are expected to yield breakthroughs in the treatment of lung cancer.

Keywords: PAD4 Inhibitor, pH response, magnetic targeting, magnetic resonance imaging, citrullination

Introduction

Lung cancer is one of the most prevalent lethal malignancies worldwide. According to recent statistics, lung cancer accounts for hundreds of thousands of deaths annually,[1,2] and this figure has shown a continuous upward trend. Current treatment modalities, including surgery, radiotherapy, and chemotherapy, have limited efficacy in the management of

Received: 24 October 2024
Accepted: 11 February 2025
Published: 12 March 2025

advanced and metastatic lung cancer.[3,4] Consequently, researchers are actively investigating novel therapeutic targets and strategies to improve the prognosis of patients with lung cancer.

Peptidylarginine deiminase 4 (PAD4) has emerged as a promising target for lung cancer therapy.[5,6] PAD4 is a post-translational modification enzyme that converts arginine residues in proteins into non-coding citrulline residues in the presence of calcium ions.[7,8] This intricate form of post-translational modification is referred to as citrullination.[9] Histones are the most extensively studied substrate for this process. Citrullination at various sites can alter interactions between DNA and other nuclear proteins, thereby modulating gene transcription and facilitating tumor progression.[10] YW403 is an established PAD4 inhibitor that effectively suppresses histone 3 citrullination and tumor growth.[11] Nevertheless, the development of PAD4 inhibitors is associated with several challenges limiting their clinical applicability, including low bioavailability, inadequate targeting specificity, and rapid metabolic degradation.[12,13]

To address these challenges, the targeted delivery of anti-cancer drugs has emerged as a crucial strategy to enhance therapeutic efficacy while minimizing adverse effects.[14] Drug targeting can be accomplished through various methodologies, including pH-responsive release, magnetic targeting carriers, and receptor targeting.[15] Among iron-based nanomaterials, iron oxide nanoparticles have been uniquely approved by the FDA for biomedical applications[16] owing to their magnetic properties, targeted delivery potential, biocompatibility, and easily modifiable surface characteristics.[17] These nanoparticles exhibit three primary characteristics: (1) They are susceptible to degradation by acidic or reducing agents, thereby facilitating controlled release.[18] (2) They exhibit responsiveness to external magnetic fields, allowing systemic administration followed by the application of external or implanted magnets to direct the magnetic nanoparticles (MNPs) to the disease or tumor site. This approach directly enhances the therapeutic dose effect in situ, thereby mitigating the potential systemic adverse reactions of chemotherapy.[19,20] (3) Additionally, these nanoparticles possess superparamagnetic iron cores, enabling their use as T2 contrast agents in magnetic resonance imaging (MRI).[21,22] This capability allows for noninvasive identification of the tissues or cells targeted by the nanoparticles.

Therefore, we designed and synthesized a PAD4 inhibitor as an iron oxide-targeted drug-delivery system. This system allowed dual-targeted drug delivery with magnetic targeting and pH-responsive release, thereby improving the efficacy and safety of PAD4 inhibitors targeting lung cancer growth and metastasis and allowing real-time monitoring through MRI. Magnetic nanocarriers were formed by the reaction of O-carboxymethyl chitosan with N-hydroxysuccinimide (NHS)/ 1-ethyl-3-(3-dimethylaminopropyl) carbodiimide (EDC), and the PAD4 inhibitor YW403 was loaded onto the magnetic nanocarriers via electrostatic action to form YW403@Fe_3O_4-oxidized carboxymethyl chitosan (OCMC) MNPs. In vitro, 3-(4,5-dimethylthiazol-2-yl)-2,5-diphenyltetrazolium bromide (MTT) and Transwell assays were used to evaluate the cytotoxic and anti-migration activities of MNPs on tumor cells. Laser confocal microscopy, cell transmission electron microscopy (TEM), Prussian blue staining, and inductively coupled plasma mass spectrometry (ICP-MS) were used to investigate the targeted uptake of the nanomedicine in vitro. The ability of the nanomedicine to induce apoptosis was investigated using flow cytometry. A mouse Lewis lung cancer metastasis model was established in vivo to evaluate the anti-tumor and anti-metastasis activities of the nanomedicine. The targeting, metabolic, and in vivo mechanisms of MNPs were investigated using immunofluorescence, ICP-MS, and MRI of mouse tumor tissue. This innovative approach is expected to provide a new and effective magnetic targeted therapeutic strategy for patients with lung cancer.

Results

Characterization of Fe_3O_4-OCMC and YW403@Fe_3O_4-OCMC MNPs

As shown in Scheme 1, the carboxyl groups on OCMC were activated using EDC and sulfo-NHS condensation methods to facilitate amide bond formation with the amino groups on the surface of the Fe_3O_4 nanoparticles, thereby chemically crosslinking OCMC to coat the surface of the Fe_3O_4 nanoparticles.[23] Subsequently, YW403, synthesized according to the literature[24] (Scheme S1, Figures S1 and S2), was encapsulated onto the surface of the Fe_3O_4-OCMC nanoparticles using the tripolyphosphate (TPP)/1% CH_3COOH method,[25] resulting in YW403@Fe_3O_4-OCMC nanoparticles. The drug-loading capacity of the Fe_3O_4-OCMC carriers was analyzed by measuring the weight change before and after drug encapsulation. The drug-loading efficiency and encapsulation efficiency of the YW403@Fe_3O_4-OCMC nanomedicine were 40.02% ± 0.96% and 33.37% ± 1.34%, respectively.

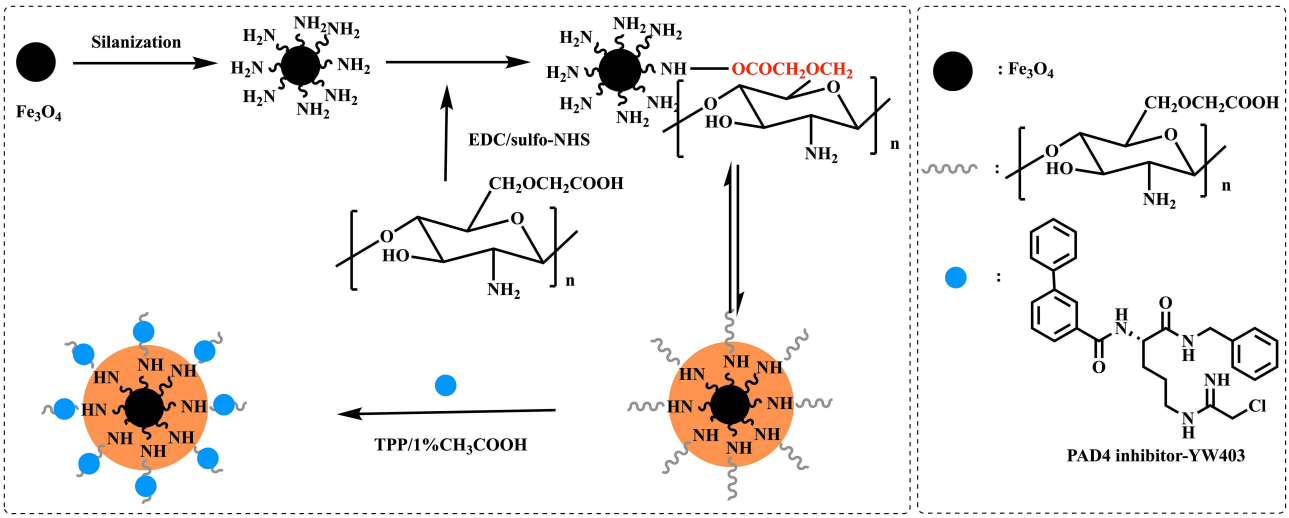

Scheme 1 Synthesis route of YW403@Fe_3O_4-OCMC.

To confirm the preparation of the nanoparticles, TEM images of Fe_3O_4-OCMC and YW403@Fe_3O_4-OCMC MNPs were recorded, and their particle sizes were statistically analyzed using ImageJ software (Figure 1A and B). Fe_3O_4, Fe_3O_4-OCMC, and YW403@Fe_3O_4-OCMC MNPs formed a uniform spherical structure, and the particle diameter gradually increased with the inclusion of chitosan and loading of YW403. Thus, the particle diameter increased from approximately 170 nm for Fe_3O_4 to 183 nm for Fe_3O_4-OCMC and 197 nm for YW403@Fe_3O_4-OCMC MNPs. This suggests that the modification of chitosan and loading of drugs increased the particle size of the iron oxide nanoparticles.

In addition, to confirm the modification of chitosan and the loading of the drug, we determined the infrared (IR) spectra of the different components (Figure S3 and Figure 1C). As shown in Figure S3, the peak at 597.76 cm^{-1} in the Fe_3O_4-OCMC spectrum is characteristic of Fe-O. The peaks at 1630.71 cm^{-1} and 3276.55 cm^{-1} represent the N-H bending vibration and O-H stretching vibration of OCMC, respectively. These characteristic peaks indicate that Fe_3O_4 and OCMC were successfully covalently connected to form Fe_3O_4-OCMC. Similarly, as shown in Figure 1C, the 595.99 cm^{-1} peak in the spectrum of YW403@Fe_3O_4-OCMC was the characteristic peak of Fe-O. The two sharp peaks at 1634.40 cm^{-1} and 1525.20 cm^{-1} were consistent with the characteristic peaks of 1633.25 cm^{-1} and 1524.93 cm^{-1} in the IR spectrum of YW403. The characteristic peak at 3057.19 cm^{-1} was consistent with the peak at 3039.33 cm^{-1} for YW403 (v_{C-H}). The presence of similar characteristic peaks indicated that YW403 was successfully loaded onto the surface of Fe_3O_4-OCMC to form YW403@Fe_3O_4-OCMC. Successful loading of YW403 was also verified by ultraviolet (UV)-vis spectroscopy. As shown in Figure 1D, YW403@Fe_3O_4-OCMC and free YW403 have the same absorption peak at 233 nm, while Fe_3O_4-OCMC had no significant absorption near 233 nm, further indicating that YW403 was successfully loaded onto the surface of Fe_3O_4-OCMC.

To further verify whether chitosan and YW403 were successfully coated onto Fe_3O_4, thermogravimetric (TG) curves and magnetization curves were obtained. As shown in Figure 1E, TG curves of Fe_3O_4 showed that Fe_3O_4 was stable in the temperature range of 30°C–1000°C, with a weight loss rate of approximately 6%. This may have been due to the loss of residual moisture in the sample. The stability of YW403 was poor; the decomposition temperature was approximately 400°C; and over 200°C–400°C, the weight loss could reach 85%. The decomposition temperature of Fe_3O_4-OCMC was approximately 700°C, and the weight loss between 200°C and 700°C was 24%, which indicated that Fe_3O_4 and OCMC are cross-linked. At the same time, the TG curve for YW403@Fe_3O_4-OCMC showed that the decomposition temperature was approximately 700°C and the weight loss rate at 200°C–700 °C was 34%, which may be due to the simultaneous degradation of YW403 and OCMC, indicating successful loading of YW403 and OCMC.

The saturation magnetization of the nanoparticles also decreased significantly, as shown in Figure 1F, from 53.78 emu/g for Fe_3O_4 to 28.4 emu/g for Fe_3O_4-OCMC and 22.4 emu/g for YW403@Fe_3O_4-OCMC, which may be due to the formation of the magnetic dead layer on the surface of the chitosan shell and the drug. In addition, X-ray crystal

https://doi.org/10.2147/IJN.S502814

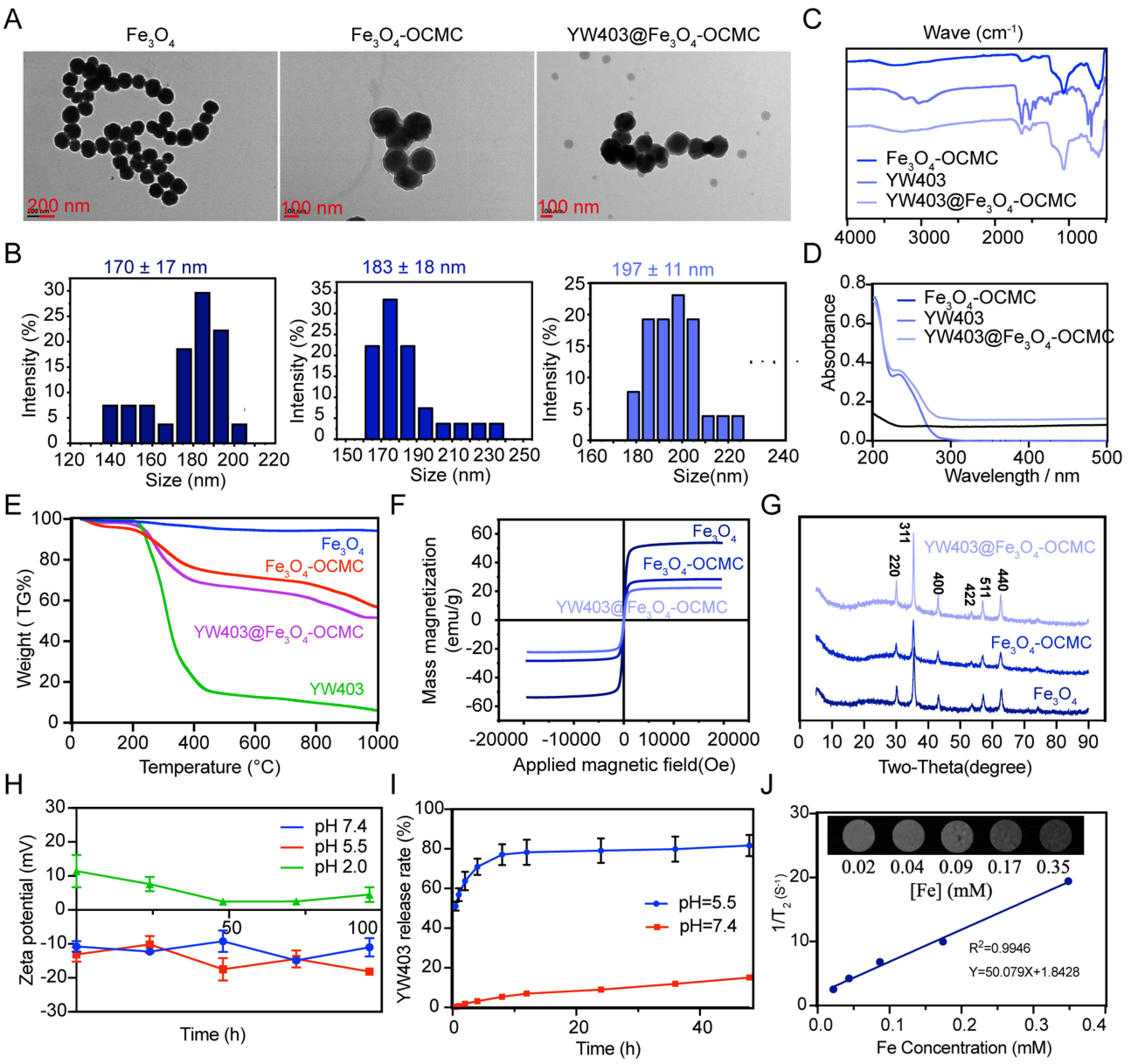

Figure 1 The characterization of Fe_3O_4, Fe_3O_4-OCMC, and YW403@Fe_3O_4-OCMC. (**A**) Transmission electron microscopy images and (**B**) diameter analysis of Fe_3O_4, Fe_3O_4-OCMC and YW403@Fe_3O_4-OCMC by ImageJ. (**C**) Infrared and (**D**) ultraviolet-vis spectra of Fe_3O_4-OCMC, YW403, and YW403@Fe_3O_4-OCMC. (**E**) Thermogravimetric analysis curves, (**F**) magnetic regression curve, and (**G**) X-ray diffraction spectrum of Fe_3O_4, Fe_3O_4-OCMC, and YW403@Fe_3O_4-OCMC. Zeta potential changes of (**H**) YW403@Fe_3O_4-OCMC and (**I**) YW403@Fe_3O_4-OCMC at 96 h in phosphate-buffered saline at different pH values (pH = 2.0, 5.5, and 7.4). (**J**) T2-weighted relaxation rates and magnetic resonance images of YW403@Fe_3O_4-OCMC at different concentrations.

diffraction spectroscopy (XRD) analysis of nanoparticles was performed. As shown in Figure 1G, six characteristic peaks of Fe_3O_4, Fe_3O_4-OCMC, and YW403@Fe_3O_4-OCMC were observed: 2θ = 30.1° (220), 35.5° (311), 43.1° (400), 53.4° (422), 57.0° (511), and 62.6° (440). The morphology of the nanoparticles did not change, suggesting that the OCMC coating and YW403 adsorption process did not cause phase transition of Fe_3O_4.

pH Stability

To evaluate the pH stability of YW403@Fe_3O_4-OCMC, zeta potential variations were continuously measured under different pH conditions (7.4, 5.5, and 2.0) for 96 h. As depicted in Figure 1H, at pH 7.4 and 5.5, the zeta potential of YW403@Fe_3O_4-OCMC remained at approximately −10 mV and exhibited minimal variation throughout the experiment, indicating that YW403@Fe_3O_4-OCMC maintained its relative stability over this time frame. Conversely, at pH 2.0, the

zeta potential shifted to positive values and gradually decreased to zero, which may be attributed to the instability of the iron oxide nanoparticles under acidic conditions, leading to their degradation into iron ions by acidic substances.

pH-Responsive Drug Release

The release of YW403 from YW403@Fe_3O_4-OCMC was measured at various pH values (5.5 and 7.4). As shown in Figure 1I, at pH 5.5, the cumulative drug release rate after 48 h was 81.74%, whereas at pH 7.4, the cumulative drug release rate was only 15.04%. This increased drug release indicated that the acidic environment promoted the release of YW403. This may be due to the lower pH, which weakens the electrostatic interaction between YW403 and the particles,[26] and may also be related to the degradation of iron oxide nanoparticles under acidic conditions.[27]

MRI Ability

Linear regression analysis was performed using the T2-weighted relaxation rate and Fe concentration of YW403@Fe_3O_4-OCMC. The concentration of iron was quantified utilizing ICP-MS, which facilitated the determination of an iron content of 31.27±4.24%. As shown in Figure 1J, and the r^2 value was 50.079 mM^{-1}•S−.[1] Moreover, MRI scans showed that the weighted image signal darkened with increasing Fe concentration. Compared to Feridex, a commercially available iron oxide-based MR contrast agent with an r^2 relaxivity of 148 mM^{-1} S^{-1}, the r^2 relaxivity of YW403@Fe_3O_4-OCMC was markedly reduced. Nonetheless, when evaluated against other surface-modified Fe_3O_4 nanoparticles, which exhibited r^2 relaxivities of 52 and 66 mM^{-1} S^{-1} respectively,[28] YW403@Fe_3O_4-OCMC retained its efficacy in MRI applications.

Cytotoxic Activity In vitro

The cytotoxic activities of Fe_3O_4-OCMC and YW403@Fe_3O_4-OCMC against the LLC, A549, and 95D tumor cell lines were evaluated using the MTT assay. To ensure the comparability of the data, the concentration of YW403 in the YW403@Fe_3O_4-OCMC group was consistent with that in the free YW403 group. As shown in Figure 2A–D, Fe_3O_4-OCMC had no significant toxic effects on the three tumor cell lines in the presence or absence of an external magnetic field. This indicates that Fe_3O_4-OCMC has good biocompatibility as a drug carrier. After administration of YW403@Fe_3O_4-OCMC, the half-maximal inhibitory concentration (IC_{50}) of the magnetic field-added group was significantly lower than that of the corresponding group without a magnetic field and the free YW403 group, indicating that the external magnetic field significantly enhanced the killing effect of the LLC, A549, and 95D tumor cell lines in the YW403@Fe_3O_4-OCMC group. This may be because the applied magnetic field increased the endocytosis of the YW403@Fe_3O_4-OCMC nanoparticles.

Cell Uptake and Distribution

The distribution of YW403-FITC@Fe_3O_4-OCMC in A549 cells was observed using laser confocal microscopy 24 h after drug administration. As shown in Figure 2E, the green fluorescence of the drug within the cells overlapped with the blue fluorescence of the cell nucleus, indicating that YW403-FITC@Fe_3O_4-OCMC was endocytosed by the A549 cells and mainly accumulated in the nucleus. Furthermore, the cellular uptake of Fe_3O_4-OCMC and YW403@Fe_3O_4-OCMC was quantified using ICP-MS in A549 cells with or without an external magnetic field. As shown in Figure 2F, the iron uptake in the group that received Fe_3O_4-OCMC with an external magnetic field was 1.67 times that in the corresponding group without an external magnetic field, while the iron uptake in the YW403@Fe_3O_4-OCMC group with an external magnetic field was 1.88 times that in the corresponding group without an external magnetic field. The results showed that the external magnetic field significantly increased the uptake of Fe_3O_4-OCMC and YW403@Fe_3O_4-OCMC by A549 cells, further explaining why the external magnetic field enhanced cellular activity.

Subcellular Localization

A549 cells were treated with YW403 and YW403@Fe_3O_4-OCMC for 24 h, and their cellular structures and nanoparticle distributions were observed using TEM. As shown in Figure 2G, the number of mitochondria in the YW403 group was significantly higher and showed obvious swelling. In the cytoplasm of the cells in the YW403@Fe_3O_4-OCMC group, a large number of vesicular structures containing metal nanoparticles were observed, but no metal nanoparticles were observed in the nucleus. This may be because YW403@Fe_3O_4-OCMC was wrapped and formed an intracellular invagination, which was then

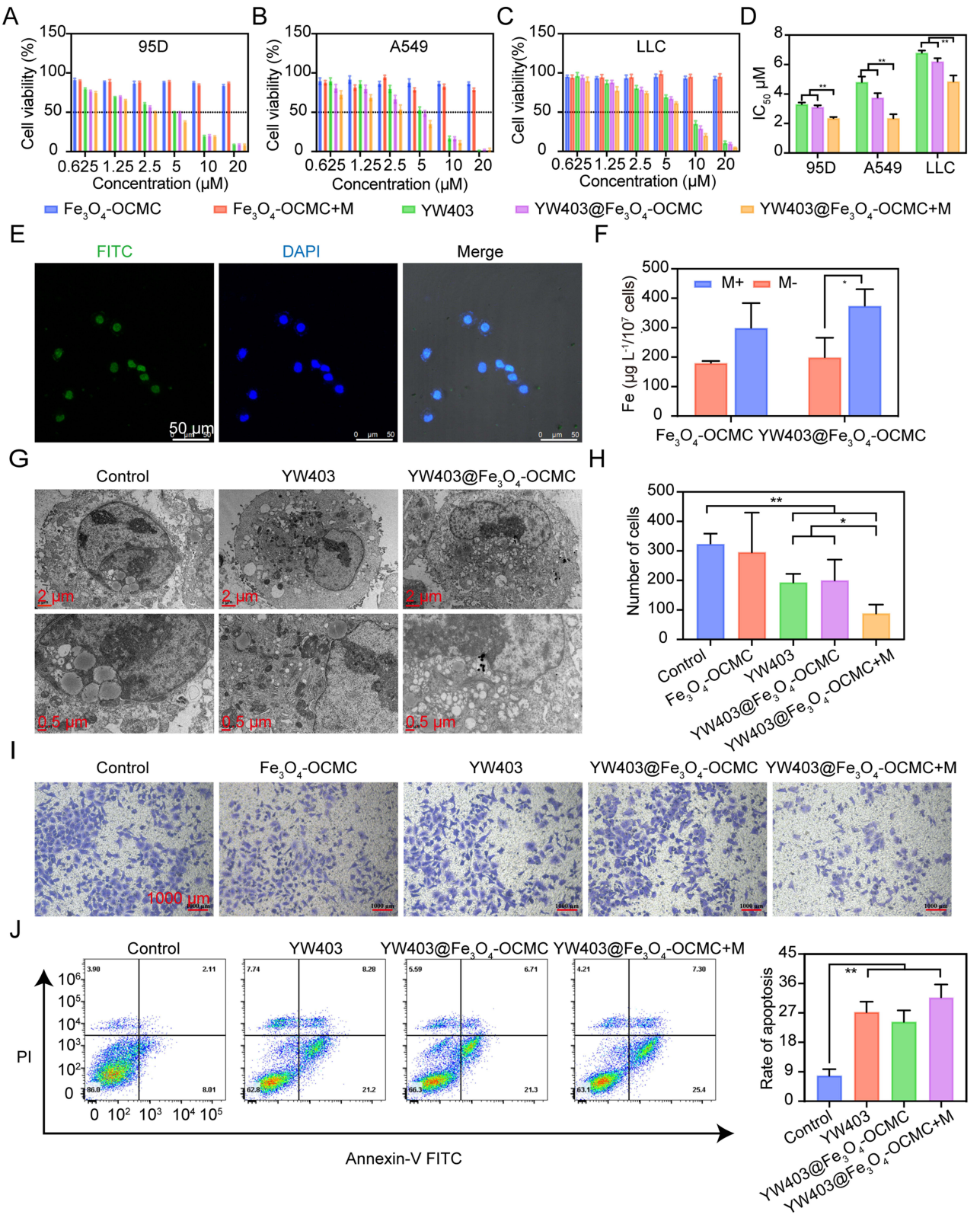

Figure 2 In vitro activity evaluation. (**A**–**C**) Viability of 95D, LLC, and A549 cells in the YW403, Fe_3O_4-OCMC, Fe_3O_4-OCMC+M, YW403@Fe_3O_4-OCMC, and Fe_3O_4-OCMC+M groups (n = 6). (**D**) Half-maximal inhibitory concentration (IC_{50}) values of YW403, YW403@Fe_3O_4-OCMC, and Fe_3O_4-OCMC+M against 95D, LLC, and A549 cells. (**E**) The distribution of YW403-FITC@Fe_3O_4-OCMC in A549 cells observed by confocal laser microscopy. (**F**) Uptake of Fe_3O_4-OCMC and YW403@Fe_3O_4-OCMC by A549 cells determined by inductively coupled plasma mass spectrometry (n = 3). (**G**) The subcellular distribution of YW403 and YW403@Fe_3O_4-OCMC in A549 cells observed by transmission electron microscopy. (**H** and **I**) A549 cell migration inhibition and statistical analysis of migration number (n = 3). (**J**) Flow cytometry and statistical analysis of A549 apoptosis induced by free YW403, YW403@Fe_3O_4-OCMC, and YW403@Fe_3O_4-OCMC+M (n = 3). * represents $P < 0.05$, ** represents $P < 0.01$.

internalized into autophagosomes for degradation, ultimately releasing iron ions and YW403. The YW403@Fe_3O_4-OCMC group exuded vesicles, indicating that YW403@Fe_3O_4-OCMC may induce apoptosis.

Anti-Metastasis Activity

The anti-migration activity of the nanoparticles toward A549 cells was assessed using the Transwell assay (Figure 2H and I). In comparison with the control group, the number of migrated cells was significantly lower in both YW403@Fe_3O_4-OCMC-treated groups, with or without an external magnetic field. However, the migration was further reduced in the presence of an external magnetic field than without a magnetic field. Thus, YW403@Fe_3O_4-OCMC effectively inhibited A549 cell migration and the magnetic field enhanced this effect.

Cell Apoptosis

The ability of YW403@Fe_3O_4-OCMC to induce apoptosis in A549 cells was determined by flow cytometry (annexin V-FITC/PI staining). As shown in Figure 2J. The apoptosis rates in the YW403, YW403@Fe_3O_4-OCMC, and YW403@Fe_3O_4-OCMC+M groups were 27.26%, 24.27%, and 31.79%, respectively. This suggests that YW403, YW403@Fe_3O_4-OCMC, and YW403@Fe_3O_4-OCMC+M induced apoptosis.

Anti-Tumor Activity In vivo

Using an LLC tumor-bearing C57BL/6 mouse model, we evaluated the effects of the nanodrugs on tumor growth and metastasis. After 11 days of treatment, as shown in Figure 3A and B, the tumor volume growth curves and weights indicated that the YW403, YW403@Fe_3O_4-OCMC, and YW403@Fe_3O_4-OCMC+M groups exhibited significantly lower tumor volumes and weights than the control group, demonstrating marked anti-tumor efficacy. Furthermore, the YW403@Fe_3O_4-OCMC+M group showed significantly smaller tumors than the YW403@Fe_3O_4-OCMC and YW403 groups, indicating that the external magnetic field enhanced the anti-tumor effect of YW403@Fe_3O_4-OCMC, likely owing to improved magnetic targeting and accumulation at the tumor site.

As shown in Figure 3C and D, the number of lung metastatic nodules in the YW403, YW403@Fe_3O_4-OCMC, and YW403@Fe_3O_4-OCMC+M groups decreased significantly. Simultaneously, the number of metastatic lung tumors in the YW403@Fe_3O_4-OCMC+M group was significantly lower than those in the YW403 and YW403@Fe_3O_4-OCMC groups, which was consistent with the HE staining in Figure 3E.This suggests that YW403@Fe_3O_4-OCMC inhibited tumor lung metastasis in vivo, and the applied magnetic field enhanced this activity.

Magnetic Targeting and Metabolism

The T2 signal in the MRI scans of the YW403@Fe_3O_4-OCMC nanomedicine decreased after the distribution of paramagnetic substances (such as iron). Therefore, the distribution of YW403@Fe_3O_4-OCMC in tumor-bearing mice was assessed by analyzing post-administration MRI signals. As illustrated in Figure 4A and B, the reduction rate of the T2 signal value within the tumors (indicated by the white circle) in the YW403@Fe_3O_4-OCMC+M group was 64.43%, which was significantly higher than that observed in the YW403@Fe_3O_4-OCMC group (23.3%). This finding suggests that the application of an external magnetic field enhanced the concentration of YW403@Fe_3O_4-OCMC within tumor tissues, potentially elucidating its role in augmenting tumor growth inhibition and suppressing metastasis under magnetic influence.

The distribution of YW403@Fe_3O_4-OCMC in tumor and normal tissues was further verified by Prussian blue staining, as shown in Figure 4C. After Prussian blue staining, the YW403@Fe_3O_4-OCMC nanoparticles aggregated in the form of blue dots in the spleen and tumor tissues, with the highest concentration in the spleen. No blue dots were detected in the heart, liver, lung, or kidney tissues, indicating that YW403@Fe_3O_4-OCMC could target tumors and metabolic tissues because of the enhanced permeability and retention (EPR) effect of the nanoparticles. To determine the iron metabolism, the iron content in the tumor and normal tissues was quantitatively determined using ICP-MS after continuous administration of the nanoparticles for 11 days and final administration of the nanoparticles for 24 h, as shown in Figure 4D. After digesting and metabolizing the tissues for 24 h, the iron was mainly concentrated in the spleen

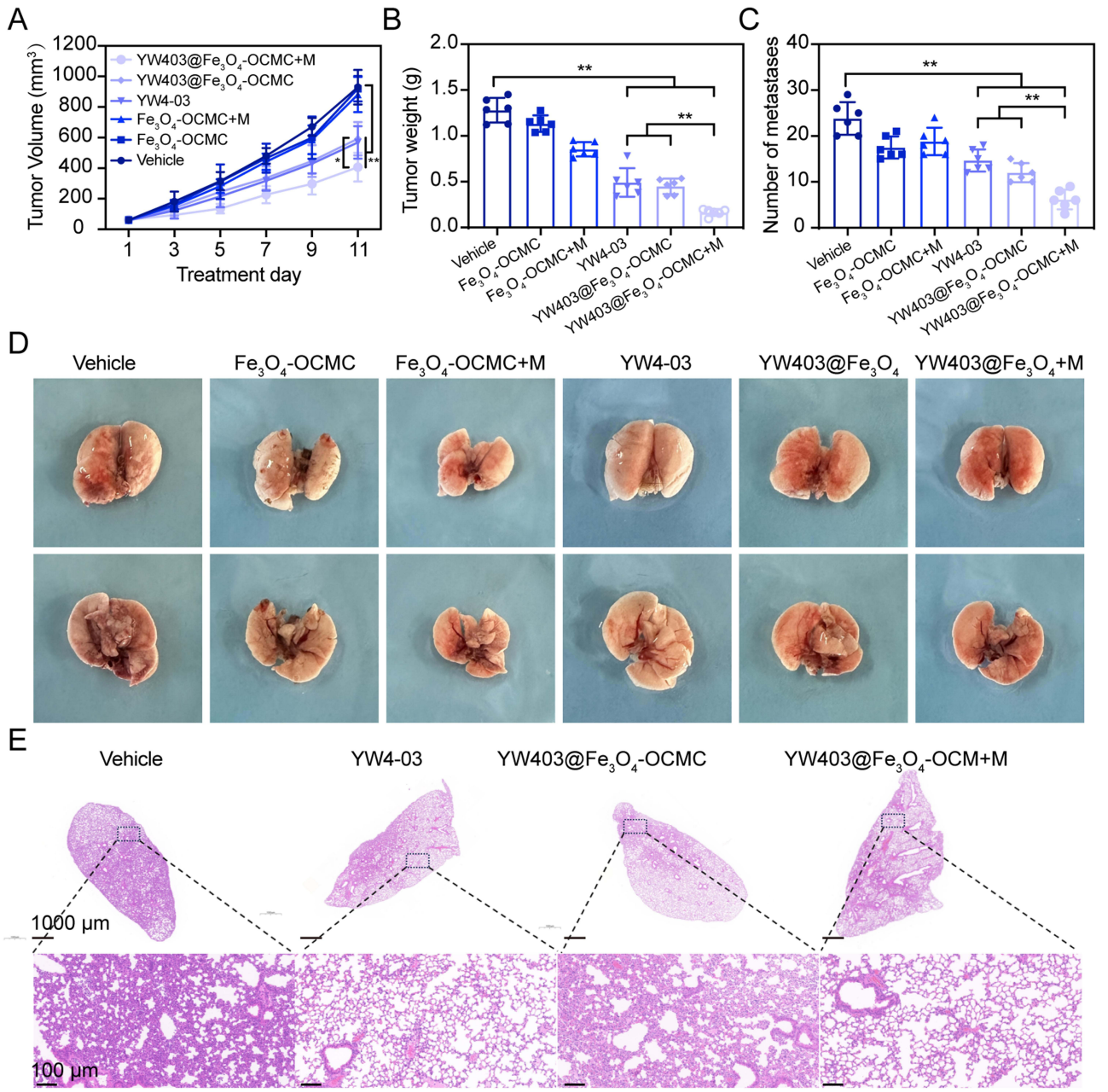

Figure 3 Inhibition of LLC tumor growth and metastasis in vivo. (**A**) Tumor volume. (**B**) Tumor weight. (**C**) Number of lung metastatic nodules. (**D**) Representative picture of lung metastasis. (**E**) Hematoxylin and eosin-stained section of lung tissue. * represents $P < 0.05$, ** represents $P < 0.01$, n = 6.

(<400 μg/g), and no significant difference was observed in the iron content between the magnetic field and non-magnetic field groups, indicating that the magnetic field did not affect iron metabolism in the body.

Metabolic Safety

To further assess the in vivo safety of YW403@Fe_3O_4-OCMC, we monitored changes in body weight, organ indices, and histological staining of the organs throughout the treatment period. As illustrated in Figure S4, the growth curves for body weight across all experimental groups during the 11-day treatment period were relatively stable, with no significant differences observed among the groups. Figure S5 presents the organ index ratios for each tested compound; no notable differences were observed between any treatment group and the vehicle control, providing preliminary evidence for the safety of this nanoparticle formulation. Additionally, Figure S6 displays hematoxylin and eosin (HE)-stained sections of

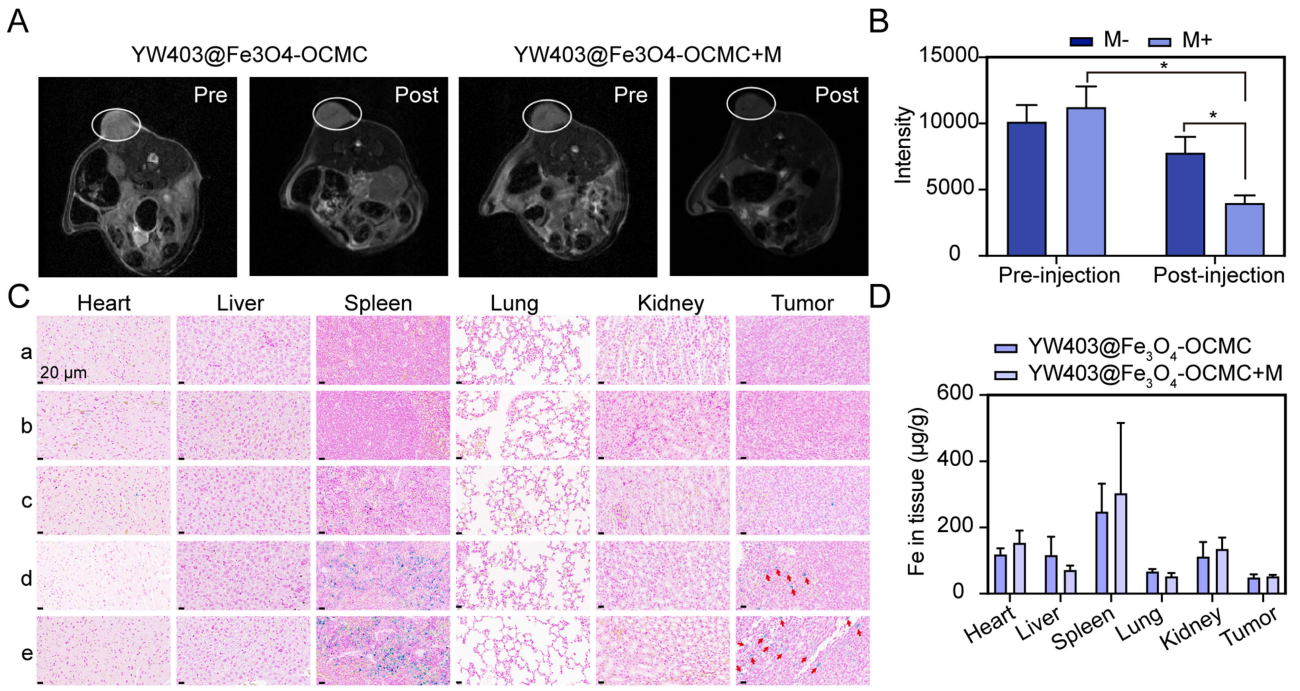

Figure 4 Magnetic imaging and magnetic targeting analysis. With or without the external magnetic field, (**A**) magnetic resonance images and (**B**) intensity analysis of YW403@Fe_3O_4-OCMC before and after single administration for 2 h. The white circles represent the tumor sites. (**C**) Prussian blue staining of mouse organ tissue: a, Vehicle; b, YW403; c, Fe_3O_4-OCMC; d, YW403@Fe_3O_4-OCMC; and e, YW403@Fe_3O_4-OCMC. The red arrows show Prussian Blue-positive cells. (**D**) After 11 days of continuous administration, the iron content in the tissue was determined by inductively coupled plasma mass spectrometry. * represents $P < 0.05$, n = 3.

organs from each test group, and the examination revealed no significant pathological or physiological alterations in the heart, liver, spleen, kidney, or brain tissue samples. These findings indicated that the YW403@Fe_3O_4-OCMC nanomedicine exhibited minimal toxicity in tumor-bearing mice.

In vivo Anti-Tumor Mechanisms

PAD4 is capable of catalyzing the citrullination of histones (H3Cit), implying that PAD4 inhibitors could reduce H3cit levels in tumors. As shown in Figure 5A and B, the average fluorescence intensity observed in the treatment groups, including the YW403, YW403@Fe_3O_4-OCMC, and YW403@Fe_3O_4-OCMC+M groups, was significantly lower than that in the Vehicle group. This finding indicated that the nanomedicine effectively inhibited the expression of H3cit in tumor tissues and that it disrupted the PAD4-H3cit pathway in tumor microenvironments, thereby inhibiting both tumor growth and metastasis.

Terminal deoxynucleotidyl transferase dUTP nick end labeling (TUNEL) staining was used to assess the capacity of YW403@Fe_3O_4-OCMC to induce apoptosis in tumor tissue cells. As illustrated in Figure 5C and D, the green fluorescence intensity observed in both the YW403@Fe_3O_4-OCMC and YW403@Fe_3O_4-OCMC+M groups was significantly greater than those in the Vehicle and Fe_3O_4-OCMC groups, indicating that YW403@Fe_3O_4-OCMC with or without a magnetic field effectively induced apoptosis in tumor cells. Furthermore, the green fluorescence intensity of the YW403@Fe_3O_4-OCMC+M group was markedly higher than those in the YW403@Fe_3O_4-OCMC and YW403 groups, suggesting that the application of an external magnetic field substantially enhanced the apoptotic induction capability of YW403@Fe_3O_4-OCMC. This finding was consistent with the cellular results presented in Figure 2D.

Methods and Materials

Materials

Fe_3O_4 (surface amino-modified, 100–200 nm) and OCMC (degree of substitution > 80%) were obtained from Shanghai Maklin Biochemical Technology Co., Ltd. LLC cells (mouse Lewis lung cancer cells), A549 cells (human non-small cell

https://doi.org/10.2147/IJN.S502814

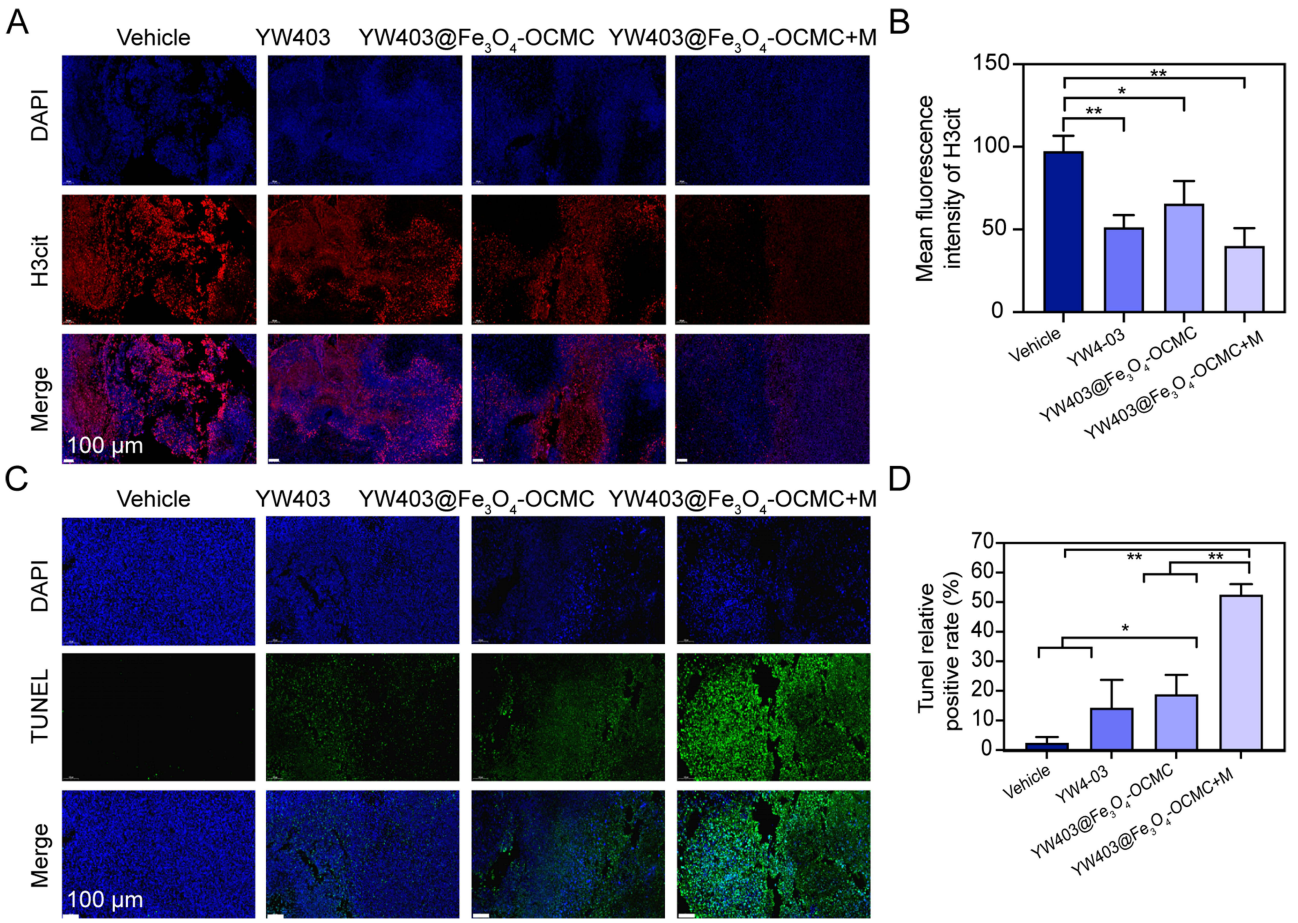

Figure 5 In vivo anti-tumor mechanisms. (**A**) Representative images of immunofluorescence sections from mouse tumor tissues and (**B**) corresponding quantitative analysis. (**C**) Representative images of terminal deoxynucleotidyl transferase dUTP nick end labeling (TUNEL)-stained sections from mouse tumor tissues and (**D**) the accompanying quantitative analysis.* represents $P < 0.05$, ** represents $P < 0.01$, n = 3.

lung cancer cells) and 95D (human high metastatic lung cancer cells) were obtained from the American Type Culture Collection (ATCC). Additional information regarding the other reagents is provided in the Supporting Information.

Preparation of Fe_3O_4-OCMC and YW403@Fe_3O_4-OCMC

The classic EDC/NHS method was employed to conjugate OCMC with the amino groups on the surface of the Fe_3O_4 nanoparticles to obtain Fe_3O_4-OCMC MNPs, as described in the Supplementary Information.

After dissolving 25 mg of Fe_3O_4-OCMC in a 1% acetic acid solution, 5 mL of YW403 aqueous solution was added at a concentration of 5 mg/mL. Subsequently, 3 mL of 0.1% sodium tripolyphosphate (STPP) solution was slowly added. The mixture was allowed to oscillate at room temperature for 4–6 h. Upon completion of the reaction, the product was washed three times with 50 mL ultrapure water to obtain the YW403@Fe_3O_4-OCMC MNPs.

In accordance with the methods outlined in the Supplementary Information, YW403@Fe_3O_4-OCMC was characterized using TEM (JEM-2100, Japan), laser nanoparticle size analysis (Nano-ZS90; Malvern Instruments Ltd., Malvern, UK), Fourier transform infrared spectroscopy (FTIR; Nicolet iS5), ultraviolet-visible spectrophotometry (UV-2600; Shimadzu, Japan), TG analysis (Mettler, Switzerland), Vibrating Sample Magnetometer (VSM; LakeShore 7404, USA), and X-ray diffraction (Rigaku SmartLab SE).

Drug Loading

The YW403 content of YW403@Fe_3O_4-OCMC was analyzed by assessing the weight change before and after drug loading. Specifically, accurately measure 25 mg of the magnetic nano-carrier Fe_3O_4-OCMC (denoted as $m_{carrier}$).

Introduce 5 mL of an aqueous YW403 solution at a concentration of 5 mg/mL (m_{drug} = C * V). YW403@Fe_3O_4-OCMC MNPs is subsequently freeze-dried. The resulting product is then weighed to determine $m_{MNPs\text{-}drug}$. The loading efficiency was calculated as follows:

$$\text{Loading Efficiency} = (m_{MNPs-drug} - m_{carrier})/m_{MNPs-drug} * 100\%$$

$$\text{Encapsulation efficiency} = \left(m_{MNPs-drug} - m_{carrier}\right)/m_{drug} * 100\%$$

In these equations, $m_{MNPs\text{-}drug}$ represents the mass of the YW403@Fe_3O_4-OCMC MNPs after drug loading, $m_{carrier}$ denotes the mass of the Fe_3O_4-OCMC carrier prior to drug incorporation, and m_{drug} indicates the mass of YW403 added.

Drug Release

To investigate the release behavior of the nanomedicine, YW403@Fe_3O_4-OCMC MNPs were dispersed in phosphate-buffered saline (PBS) solutions with pH values of 7.4 and 5.5, and placed in a 37°C water bath for agitation release. UV-vis absorbance at 233 nm was measured at predetermined time intervals (0.5, 1, 2, 4, 8, 12, 24, 36, and 48 h) to monitor the release behavior.

In vivo Activity Assay

Male C57BL/6N mice (20 ± 2 g) were obtained from Beijing Weitong Lihua Laboratory Animal Technology Co. The animal study was approved by the Institutional Animal Care and Use Committee of the Capital Medical University (approval number: AEEI-2018-174). Lung cancer cells (LLC) were inoculated subcutaneously into mice until the average tumor volume reached 50–100 mm^3. Tumor-bearing mice were randomly divided into six treatment groups: Vehicle, Fe_3O_4-OCMC, Fe_3O_4-OCMC+M, YW403, YW403@Fe_3O_4-OCMC, and YW403@Fe_3O_4-OCMC+M. The dosage for the YW403 group was set at 10 μmol/kg while maintaining consistent dosages of YW403 in both the YW403@Fe_3O_4-OCMC and YW403@Fe_3O_4-OCMC+M groups compared to free YW403; the dosages for Fe_3O_4-OCMC and Fe_3O_4-OCMC+M groups matched that of the Fe_3O_4 in the YW403@Fe_3O_4-OCMC MNPs group. Each treatment group consisted of six mice, with all administered volumes calculated as 0.1 mL/10 g body weight and administered via intraperitoneal injection (i.p.) once daily for a total duration of 11 days. In addition, a magnetic field was applied by placing a small NdFeB permanent magnet (15 mm × 5 mm cylinder with a surface magnetic field strength of 0.5 T) over the abdomen for 0.5 h after administration.

During treatment, the tumor volume and mouse body weight were monitored regularly. Twelve hours after the final administration, the weights of the mice were recorded before euthanasia under isoflurane anesthesia. Fresh blood samples (1 mL) were collected for serum biochemical analysis after centrifugation of the supernatants. Organs, including the heart, liver, spleen, lungs, and kidneys, and tumors were immediately dissected, weighed, and photographed. Three sets of organs and tumors were preserved at −80°C, while the other three sets underwent fixation in 4% paraformaldehyde.

Tumor volume was calculated using the formula:

Tumor volume (V) = a^2*b/2 (where a and b were the shortest and longest diameters of a given tumor, respectively).

Magnetic Resonance Imaging In vivo

The tumor-bearing mice were immobilized and placed in an MRI system (Bruker, Germany) for imaging. T2-weighted MR images were acquired using a multi-echo multi-slice (MEMS) spin echo sequence with the following parameters: TR/TE = 3000/22.5 ms, 256×256 matrices, 35×35 mm field of view, and a slice thickness of 0.70 mm. After imaging, the mice were intraperitoneally administered YW403@Fe_3O_4-OCMC, and a small NdFeB permanent magnet (15 mm × 5 mm cylinder; surface magnetic field, 0.5 T) was placed at the tumor site of the mice in the YW403@Fe_3O_4-OCMC+M group for 0.5 h. After 1.5 h, the mice were taken and placed in the MRI system for imaging.

Statistical Analysis

All data are presented as mean ± standard deviation and were analyzed using one-way analysis of variance (ANOVA) or *t*-tests with Prism 8.0 software. Values were derived from a minimum of three independent experiments. Statistical significance was considered at a p-value of <0.05, while a p-value of <0.01 indicated an extremely significant difference.

Conclusion and Discussion

In this study, a magnetic nanocarrier composed of Fe_3O_4 and OCMC was used as the primary material. Using electrostatic adsorption, the PAD4 inhibitor YW403 was loaded onto the magnetic nanocarrier Fe_3O_4-OCMC, yielding a magnetically targeted nanomedicine, YW403@Fe_3O_4-OCMC. This innovative system integrated magnetic targeting, pH-responsive release, and MRI to create a highly efficient targeted drug-delivery platform that could enhance the therapeutic efficacy of PAD4 inhibitors while improving drug safety.

In vitro cytotoxicity assays demonstrated that the Fe_3O_4-OCMC nanocarriers exhibited low toxicity even under external magnetic field conditions, indicating excellent biocompatibility. The inhibitory effects of YW403@Fe_3O_4-OCMC MNPs on the three types of tumor cells were dose-dependent. Moreover, application of an external magnetic field significantly enhanced the inhibitory capacity against tumor cells. MRI suggested that this enhancement may result from the increased uptake of YW403@Fe_3O_4-OCMC MNPs by A549 tumor cells owing to the influence of the external magnetic field.

In vivo studies revealed that YW403@Fe_3O_4-OCMC MNPs significantly inhibited tumor growth and metastasis in Lewis lung cancer mice by suppressing H3cit expression when subjected to an external magnetic field. This indicated effective magnetic targeting with minimal biological toxicity. Furthermore, YW403@Fe_3O_4-OCMC induced apoptosis in tumor cells, corroborating previous findings. Finally, we investigated the absorption and metabolism profiles of YW403@Fe_3O_4-OCMC MNPs in mice and observed a predominant distribution within the spleen and reduced biological toxicity.

Collectively, our findings indicated that YW403@Fe_3O_4-OCMC MNPs facilitated targeted drug delivery under an external magnetic field. In comparison to other currently available magnetic nanoparticles utilized for therapeutic purposes,[29,30] YW403@Fe_3O_4-OCMC MNPs maintain the functionalities of magnetic resonance imaging and magnetic targeting, while also enhancing the biocompatibility of these nanoparticles with tissue. Furthermore, YW403@Fe_3O_4-OCMC MNPs exhibit dual functionalities in inhibiting both tumor growth and metastasis. Significantly, these nanoparticles enhance the endocytic uptake of drugs by tumor cells and achieve nuclear penetration. This provides new insights for the development of novel anti-tumor nanomedicines.

Data Sharing Statement

Materials and protocols will be distributed to qualified scientific researchers for noncommercial and academic purposes.

Acknowledgments

The authors acknowledge the facilities supported by the Research and Development Laboratory of Innovative Drugs for Metabolic Diseases of the Capital Medical University (Beijing, China).

Author Contributions

All authors made a significant contribution to the work reported, whether that is in the conception, study design, execution, acquisition of data, analysis and interpretation, or in all these areas; took part in drafting, revising or critically reviewing the article; gave final approval of the version to be published; have agreed on the journal to which the article has been submitted; and agree to be accountable for all aspects of the work.

Funding

This study is supported by National High Level Hospital Clinical Research Funding under Grant BJ-2023-100, the Chinese Institutes for Medical Research, Beijing under the CIMR Organized Scientific Research Program (CX23YZ06), the National Natural Science Foundation of China for Young Scholars (No. 22407094), and the R&D Program of Beijing Municipal Education Commission (KM202410025024).

Disclosure

The authors declare no competing financial interests.

References

1. World Health Organization. Global cancer burden growing, amidst mounting need for services. *Saudi Med J*. 2024;45(3):326–327.
2. Sung H, Ferlay J, Siegel RL, et al. Global Cancer Statistics 2020: GLOBOCAN Estimates of Incidence and Mortality Worldwide for 36 Cancers in 185 Countries. *CA Cancer J Clin*. 2021;71(3):209–249. doi:10.3322/caac.21660
3. Abu Rous F, Singhi EK, Sridhar A, Faisal MS, Desai A. Lung Cancer Treatment Advances in 2022. *Cancer Invest*. 2023;41(1):12–24. doi:10.1080/07357907.2022.2119479
4. Girigoswami A, Girigoswami K. Potential Applications of Nanoparticles in Improving the Outcome of Lung Cancer Treatment. *Genes (Basel)*. 2023;14(7):1370. doi:10.3390/genes14071370
5. Wu X, Chan L, Zhu D, Pang Y, Jin M, Wang Y. Mitosis targeting in non-small lung cancer cells by inhibition of PAD4. *Heliyon*. 2024;10(6):e27313. doi:10.1016/j.heliyon.2024.e27313
6. Baka Z, Barta P, Losonczy G, et al. Specific expression of PAD4 and citrullinated proteins in lung cancer is not associated with anti-CCP antibody production. *Int Immunol*. 2011;23(6):405–414. doi:10.1093/intimm/dxr026
7. Alghamdi M, Al Ghamdi KA, Khan RH, Uversky VN, Redwan EM. An interplay of structure and intrinsic disorder in the functionality of peptidylarginine deiminases, a family of key autoimmunity-related enzymes. *Cell mol Life Sci*. 2019;76(23):4635–4662.
8. Wang Y, Chen R, Gan Y, Ying S. The roles of PAD2- and PAD4-mediated protein citrullination catalysis in cancers. *Int J Cancer*. 2021;148(2):267–276. doi:10.1002/ijc.33205
9. Wang Y, Wysocka J, Sayegh JR, et al. Human PAD4 regulates histone arginine methylation levels via demethylimination. *Science*. 2004;306(5694):279–283. doi:10.1126/science.1101400
10. Zhu D. PAD4 and Its Inhibitors in Cancer Progression and Prognosis. *Pharmaceutics*. 2022;14(11):2414.
11. Wang Y, Li P, Wang S, et al. Anticancer peptidylarginine deiminase (PAD) inhibitors regulate the autophagy flux and the mammalian target of rapamycin complex 1 activity. *J Biol Chem*. 2012;287(31):25941–25953. doi:10.1074/jbc.M112.375725
12. Lu Y, Peng Z, Zhu D, et al. RGD Peptide and PAD4 Inhibitor-Loaded Gold Nanorods for Chemo-Photothermal Combined Therapy to Inhibit Tumor Growth, Prevent Lung Metastasis and Improve Biosafety. *Int J Nanomed*. 2021;16:5565–5580. doi:10.2147/IJN.S319210
13. Zhu D, Lu Y, Hu B, et al. Highly-tumor-targeted PAD4 inhibitors with PBA modification inhibit tumors in vivo by specifically inhibiting the PAD4-H3cit-NETs pathway in neutrophils. *Eur J Med Chem*. 2023;258:115619. doi:10.1016/j.ejmech.2023.115619
14. Shao D, Li J, Zheng X, et al. Janus "nano-bullets" for magnetic targeting liver cancer chemotherapy. *Biomaterials*. 2016;100:118–133. doi:10.1016/j.biomaterials.2016.05.030
15. Ashique S, Sandhu NK, Chawla V. Targeted Drug Delivery: trends and Perspectives. *Curr Drug Deliv*. 2021;18(10):1435–1455.
16. Chen Q, Liu L, Lu Y, et al. Tumor Microenvironment-Triggered Aggregated Magnetic Nanoparticles for Reinforced Image-Guided Immunogenic Chemotherapy. *Adv Sci*. 2019;6(6):1802134. doi:10.1002/advs.201802134
17. Farzin A, Etesami SA, Quint J, Memic A, Tamayol A. Magnetic Nanoparticles in Cancer Therapy and Diagnosis. *Adv Healthc Mater*. 2020;9(9):e1901058. doi:10.1002/adhm.201901058
18. Shen Z, Song J, Yung BC, Zhou Z, Wu A, Chen X. Emerging Strategies of Cancer Therapy Based on Ferroptosis. *Adv Mater*. 2018;30(12):1704007.
19. Chen L, Zhong H, Qi X, Shao H, Xu K. Modified core-shell magnetic mesoporous zirconia nanoparticles formed through a facile "outside-to-inside" way for CT/MRI dual-modal imaging and magnetic targeting cancer chemotherapy. *RSC Adv*. 2019;9(23):13220–13233. doi:10.1039/C9RA01063G
20. Xu Y, Li W, Chen S, Huang B, Pei W, Niu C. Near-Infrared Responsive Phase-Shifted Nanoparticles for Magnetically Targeted MR/US Imaging and Photothermal Therapy of Cancer. *Front Bioeng Biotechnol*. 2020;8:599107. doi:10.3389/fbioe.2020.599107
21. Ren S, Song L, Tian Y, et al. Emodin-Conjugated PEGylation of Fe3O4 Nanoparticles for FI/MRI Dual-Modal Imaging and Therapy in Pancreatic Cancer. *Int J Nanomed*. 2021;16:7463–7478. doi:10.2147/IJN.S335588
22. Wang C, Yan C, An L, Zhao H, Song S, Yang S. Fe_3O_4 assembly for tumor accurate diagnosis by endogenous GSH responsive T2/T1 magnetic relaxation conversion. *J Mater Chem B*. 2021;9(37):7734–7740. doi:10.1039/D1TB01018B
23. Rizeq BR, Younes NN, Rasool K, Nasrallah GK. Synthesis, Bioapplications, and Toxicity Evaluation of Chitosan-Based Nanoparticles. *Int J mol Sci*. 2019;20(22):5776. doi:10.3390/ijms20225776
24. Jones JE, Slack JL, Fang P, et al. Synthesis and screening of a haloacetamidine containing library to identify PAD4 selective inhibitors. *ACS Chem Biol*. 2012;7(1):160–165. doi:10.1021/cb200258q
25. Zou X, Wang Q, Li H, Wang Q, Li H. Preparation and drug release behavior of pH-responsive bovine serum albumin-loaded chitosan microspheres. *J Ind Eng Chem*. 2015;21:1389–1397. doi:10.1016/j.jiec.2014.06.012
26. Sobierajska P, Serwotka-Suszczak A, Targonska S, Szymanski D, Marycz K, Wiglusz RJ. Synergistic Effect of Toceranib and Nanohydroxyapatite as a Drug Delivery Platform-Physicochemical Properties and In Vitro Studies on Mastocytoma Cells. *Int J mol Sci*. 2022;23(4):1944. doi:10.3390/ijms23041944
27. Ren Z, Sun S, Cui G, et al. A Metal-Polyphenol-Coordinated Nanomedicine for Synergistic Cascade Cancer Chemotherapy and Chemodynamic Therapy. *Adv Mater*. 2020;32(6):e1906024. doi:10.1002/adma.201906024
28. Patel D, Kell A, Lin HY, Tian G, Lin HY, Tian G. The cell labeling efficacy, cytotoxicity and relaxivity of copper-activated MRI/PET imaging contrast agents. *Biomaterials*. 2011;32(4):1167–1176. doi:10.1016/j.biomaterials.2010.10.013
29. Gowtham P, Girigoswami K, Pallavi P, Harini K, Gurubharath I, Girigoswami A. Alginate-Derivative Encapsulated Carbon Coated Manganese-Ferrite Nanodots for Multimodal Medical Imaging. *Pharmaceutics*. 2022;14(12):2550. doi:10.3390/pharmaceutics14122550
30. Mishra S, Yadav MD. Magnetic Nanoparticles: a Comprehensive Review from Synthesis to Biomedical Frontiers. *Langmuir*. 2024;40(33):17239–17269.